Etch Profile Control of High-Aspect Ratio, Deep Submicron α-Si Gate Etch

H.-M. Park*

Intel Components Research,
RA1-204 5200 NE Elam Young Parkway
Hillsboro, OR 97124-6497, USA

D. S. Grimard, J. W. Grizzle, and F. L. Terry, Jr.

Electronics Manufacturing and Control Systems Laboratory,
Dept. of Electrical Engineering and Computer Science, University of Michigan, Ann Arbor, MI 48109-2122, USA

ABSTRACT

The well-acknowledged etch profile drift problem in chip production was investigated with a more accurate means of measuring actual etch thickness to monitor and correct this drift. Using a high-aspect ratio, 0.1 μm α-Si gate structure, the investigation was specifically focused on the control of transition timing in the critical interval from main etch (ME) to over etch (OE). This required reliable endpoint detection of α-Si which was achieved through the development of a method employing a Kalman-Bucy filter with a real-time spectroscopic ellipsometer (RTSE). The robustness of our endpoint detection technique was tested and demonstrated under the actual physical and chemical disturbance environments of the etching process. Application of this endpoint detection technique to the etch of a 0.1 μm patterned α-Si gate also achieved a significant improvement on the etch profile repeatability.

*Author to whom correspondence should be addressed. Tel: 503-613-9663, Fax: 503-613-7189, email: hyun-mog.park@intel.com

I. Introduction

The drive to miniaturize device feature size has exerted tremendous pressure on research to design and produce smaller chips which are both highly reliable and cost-effective. Though the reduction of chip size is governed by Moore's law, the miniaturization itself has given rise to a whole new set of problems that are roughly inversely proportional to the reduction in chip size. Considerable energy has been focused on improving hardware, materials, processes, and measurements in an attempt to enhance productivity in a highly competitive industry. Among these challenges, the etching process, a fundamental stage in the chip production, has proven to be particularly troublesome, especially in the light of ever tightening production tolerances. Because the etching process is irreversible, developing a highly stable etching process that can be precisely controlled in response to the increasing demands of miniaturization becomes crucial, from both the point of profitability and manufactuability. At present, the decrease in device feature size, and the increase in aspect ratio and wafer size have made it increasingly difficult to achieve a flawless etch. Increased wafer size is a particular challenge to the production of a highly uniform etch. With the decrease of gate oxide thickness, a highly selective low-damage etch is critical. The current solutions to these etch process problems can be roughly categorized into three areas: a) process development and optimization, b) hardware development, and c) process modeling and control [1–8].

In this study, we tackle two critical etch process problems, etch rate drift and etch profile drift, through real-time, closed-loop process control. Etch rate drift can result in significant production delay and cost by making it necessary to run more pilot wafers and pre-production trials to adjust an etch recipe for final production use. Figure 1 illustrates long-term (over eight months) and short-term (within one hour) α-Si etch rate variation observed in a Lam TCP 9400SE plasma etching system. Despite relatively low run-times and frequent chamber cleaning, we observed a 29.4 nm etch rate drift (3σ) over eight months of etching. The nominal etch rate was 207 nm/min. Though the short-term etch rate drift we documented is relatively insignificant compared to the long-term drift, it is, nonetheless, evidence of the need for real-time process control. On the other hand, variations in the etch profile, day-by-day or lot-by-lot, can directly influence device speed to the point of exceeding device tolerance [9, 10]. Moreover, the drive to improve device speed has led to significant reduction of critical dimension (CD) tolerance in gate production. In short, it has become increasingly critical to maintain the consistency of production runs at very tight tolerances.

Figure 2 shows the cross-sectional etch profile of 0.1 μm α-Si gate structures after 10/75/90 sec

of breakthrough/main etch/over etch in a Lam TCP 9400SE plasma etching system. Although two identical samples were etched 10 days apart under identical etch conditions, a clear etch profile difference was evident. With the increased production cost in semiconductor manufacturing, unidentified and un-corrected process problems result in significant production cost. Thus, it is critical to study a means for the real-time detection and correction of etch rate and etch profile variations.

In this paper, we propose to control etch profile drift by regulating the transition timing from main etch (ME) to over etch (OE). This is achieved utilizing a real-time spectroscopic ellipsometer (RTSE) in combination with a Kalman-Bucy filter to estimate real-time film thickness. The experimental details will be presented in Section II, together with a description of the plasma etching system, the RTSE, and the sample preparation. Section III details the development of a 0.1 μm α-Si gate etch process and preliminary experimental results of the 0.1 μm patterned sample etch. The ME endpoint detection technique developed using a Kalman-Bucy filter is described in Section IV. Finally, Section V examines application of this control method to etch a patterned sample. We conclude with a summary in Section VI.

II. Experimental Details

A low-pressure, high-plasma density Lam TCP 9400SE plasma etching system with a RTSE were used in our experiment. A brief description of the equipment and a 0.1 μm oxide etch mask patterning procedure will be given.

A. Hardware

A.1 The Plasma Etching System: Lam TCP 9400SE

For the etch of a deep sub-micron patterned wafer, a low-pressure, high-plasma density Lam TCP 9400SE etcher was used (Fig. 3). As a dual-power-source etcher, the TCP 9400SE employs a "transformer coupled" RF power supply to set plasma density and a standard capacitively coupled RF "bias" power supply to set ion energy. To maximize the delivered power to the plasma reactor and protect the power supplies and cables, a matching network is connected to the power source and electrode. The etcher is equipped with a six-inch bipolar electrostatic chuck with helium backside cooling. The temperature controller of the bottom electrode was set to 60 C and chamber temperature to 50 C throughout the experiment. This plasma etcher is designed for six-inch or eight-inch wafers with sub-half-micron pattern etch of poly-Si, refractory metal silicides, organic anti-reflection coating (ARC),

nitride, and cured photoresist, and thus, C_2F_6, Cl_2, HBr, SF_6, O_2, He, and N_2 gases are supplied. The TCP 9400SE etcher has two built-in photodiode endpoint detectors based on optical emission spectroscopy (OES): 405 and 520 nm wavelength bandpass OES sensors. The 405 nm wavelength matches the SiN and AlCl emission lines, whereas the 520 nm matches the C_2, CO, SiCl, and O_2 emission lines. To minimize disturbance from the process chamber being exposed to the atmosphere and absorbing water vapor, an entrance and exit loadlock are provided. To acquire data and control the etching process, a PC running LabVIEW was piggybacked onto the Nvision system, which is an original operating system of the Lam TCP 9400SE [11]. A custom LabVIEW-based control program, EMACS, is monitors and controls the etching process, while other processes, such as wafer loading/unloading, pumping, and venting, are operated by Lam's Nvision system.

A.2 Real-Time Spectroscopic Ellipsometer

Ellipsometry is an optical technique that measures changes in the polarization state of light reflected from a surface. The major advantages of ellipsometry are its non-destructive nature, high sensitivity, large measurement range (from fractions of monolayers to micrometers), and possible real-time implementation. Ellipsometry has been used extensively for *in situ* film thickness and etch rate measurement [12–14], film characterization [15], and in-line monitoring of repetitive patterns [16]. A reflection ellipsometer measures the states of the incident and reflected waves, leading to the determination of the ratio ρ of the complex Fresnel reflection coefficients for the parallel (subscript p) and perpendicular (subscript s) polarizations [17]:

$$\rho = (r_p/r_s) = \tan(\Psi)\exp(i\Delta). \tag{1}$$

The measured complex ratio is usually expressed in terms of the ellipsometric variables, Ψ and Δ, where $\tan(\Psi)$ corresponds to the attenuation and Δ to the phase shift between the two components. From these data, the complex index of refraction and film thickness can be determined using a computer model fit. With the assumption that the ambient is air, the reflectance coefficients are directly related to the optical constants of the surface:

$$r_p = \frac{n\cos\phi_i - \cos\psi_i}{n\cos\phi_i + \cos\psi_i} r_s = \frac{\cos\phi_i - n\cos\psi_i}{\cos\phi_i + n\cos\psi_i} \tag{2}$$

where n is the complex refractive index $n = N - iK$ of the surface.

A commercial RTSE was installed on the Lam TCP 9400SE etching system. For the installation, two small view ports were built in the sidewall of the etch chamber. The light source of the RTSE

is a high-pressure Xe arc lamp with an approximate 5 mm beam diameter and intensified photodiode array (IPDA) with controller (a DSP board in a PC) that detects the reflected wave from the surface. The spectral range of the RTSE is 1.8-4.5 eV (approximately 220-560 nm) with 512 pixels for high resolution. The measurement speed is typically 10Hz with 10 turns/sec for the polarizer. Extraction of the thickness information from the collected ellipsometric data is usually done by the "WinElli" program. However, the "WinElli" is an *ex situ* film thickness fitting program. Thus, the "FitRTSE" program was used instead, and run with the ellipsometric data collection. This program fits collected ellipsometric data to the optical model of the film under measurement in real time.

B. Sample Preparation

In order to study deep submicron etch, we needed a sample patterned with sufficiently small features. To that end, our samples consisted of a 100-nm thick oxide etch mask over 200 nm of phosphorus-doped (n-doped) α-Si (respectively, 400 nm) on a thermally grown 5-nm thick gate oxide. α-Si was employed for the gate material because its amorphous structure reduces after-etch surface roughness of the gate sidewall. The process flow of the 100-nm oxide etch mask patterning step is illustrated in Fig. 4. The 100-nm thick oxide etch mask was patterned using direct exposure electron-beam lithography (EBL) and a lift-off process. A positive e-beam resist, polymethylmethacrylate (PMMA), with a surface-linking promoter, hexamethyldisilazane (HMDS), was spin-coated. To improve the adhesion of the resist and anneal the stresses caused by the shear forces encountered in the spinning process, 30 min of 180 C pre-bake was followed. After the pre-bake, the wafer was processed with a 1:3 ratio of methyl isobutyl ketone (MIBK): iso propyl alcohol(IPA) developer for 2 min. This was followed by the electron-beam evaporation of oxide for the hard etch mask patterning. We selected oxide evaporation over thermal oxide growth because of its compatibility with the lift-off process at the expense of its relatively lower etch selectivity over silicon. For future reference, it is worth noting that the cross-sectional profile of the oxide etch mask after the lift-off process is triangular rather than rectangular (Fig. 5). To investigate the potential effects of microloading during the etching process, both isolated (1:3 and 1:10 line-to-space ratio) and nested gate-lines (1:1 line-to-space ratio) were patterned on a four-inch wafer. In this research, a 2×2 cm patterned sample was used instead of a whole wafer due the well-known problem of long exposure time with EBL. The sample was introduced into the etcher via a carrier wafer: each sample was mounted on a six-inch silicon wafer via vacuum grease, and then etched. We used a Philips XL 30 FEG scanning electron microscope (SEM) to evaluate the etch profile

of the sample after etch.

III. Etch Process Development and the Importance of ME to OE Transition Timing

We used a three-step etch recipe consisting of BT, ME, and OE, with chlorine and bromine process gases. The BT step etches a thin layer of native oxide from a wafer surface by employing C_2F_6. Since the subsequent ME is highly selective to oxide, this BT step is critical in preventing micromasking. To improve etch rate and minimize undercut, a chlorine and bromine gas mix was used in the ME step [1, 2]. The OE step was designed to achieve a very high etch selectivity over oxide (more than 100:1) utilizing mild ion bombardment to minimize gate oxide loss and damage. HBr was used to maintain a highly anisotropic etch profile in the OE. Since a bromine plasma has a tendency to form localized discharges under reactive ion etching (RIE) plasma condition, helium was added to dilute the HBr [18]. The noble helium gas has little affect on the surface process that determines the silicon etching characteristics. O_2 was also mixed to improve the etch selectivity of α-Si with respect to silicon dioxide. The details of the etch recipe are shown in Table I. The ME and OE recipe were adopted from the Bell Labs recipe [19]; however, our plasma etching system is equipped with a small vacuum pump (1000 ℓ/sec), forcing us to cut the ME gas flow rate in half. Despite the reduced gas flow, we were only able to maintain a 10 mTorr chamber pressure which is substantially higher than the 2 mTorr of Bell Labs.

To increase throughput, the majority of gate material near the gate oxide is etched during the high etch rate ME stage, leaving the residual gate material to be etched under the highly selective OE stage as illustrated in Fig. 6. However, in our experiment, the oxide etch mask was close to triangular since an electron-beam evaporation and lift-off process was used. Because of this etch mask shape, the low evaporated oxide etch selectivity to α-Si, and the high-aspect ratio, the ME had to be terminated when only half of the gate was etched so as to preserve the integrity of the etch mask.

To investigate the effect of ME and OE on the etch profile of our high-aspect ratio gate structure, two sets of experiments were conducted. In the first set, 10 sec of BT was followed by each of 45, 60, and 75 sec of ME, without the OE step; whereas, in the second set, 10 sec of BT was followed by each of 80, 100, and 120 sec of OE, with no ME step. To facilitate etch profile comparison, the OE etch time was set to etch the same etch depth of α-Si as in the ME. Figure 7 illustrates the cross-sectional etch profiles of each experiment. The samples were dipped in buffered hydrofluoric acid (BHF) solution for 10 sec after the etch to remove any residual oxide etch mask or re-deposited oxide-like materials

on the sidewall. There was a clear difference observed in the etch profile achieved in the ME with its intensive ion bombardment, compared to that of the OE with more mild ion bombardment geared to improve etch selectivity. A prolonged ME caused the loss of gate oxide and produced a narrower gate structure due to the loss of etch mask integrity. In the OE, on the other hand, the re-deposition of etch products on the wafer surface with mild ion bombardment contributed to the deterioration of the etch mask pattern transfer. This, in turn, increased the gate width.

We next examined what affect time variations in the ME would have on the final etch profile. To do so, we conducted the following experiment. After 10 sec of BT to etch the native oxide, one sample was subject to 45 sec of ME, whereas the other sample was subject to 60 sec. Then, both samples underwent 120 sec of OE to etch any residual α-Si materials. The cross-sectional etch profiles of the two samples are presented in Fig. 8. The 60 sec of ME caused greater erosion of the oxide etch mask resulting in a narrower gate top and a wider space between gate structures. At 45 sec of ME, the average CD for the top of the dense gate lines was 67 nm, as opposed to 55 nm at 60 sec of ME. In addition, at 45 sec of ME, the space at the foot of the gate between adjacent gate structures proved to be wider than at 60 sec of ME (125 nm as compared to 110 nm). It is evident from this experiment that in terms of the amount of gate material etched, the ME is crucial to the final etch profile. Moreover, it becomes obvious that the conventional timed etch in the presence of severe etch rate drift can seriously compromise production consistency.

IV. Development of Endpoint Detection Algorithm

Once it becomes evident that the transition timing from ME to OE is a critical stage in maintaining an etch profile, the next task is to develop a system that can accurately determine the transition timing from ME to OE. This, however, requires measurement of film thickness variation with very fine resolution. To this end, we employed a RTSE system to measure the real-time film thickness of the gate material during the etching process. Unfortunately, due to the limited detection range of the RTSE setup at the University of Michigan, we could not measure the α-Si thickness in real time. Therefore, we measured the film thickness of a 2×2 cm n-doped poly-Si sample placed in the center of the six-inch Si carrier wafer [13]. Assuming constant etch selectivity of poly-Si over α-Si, the measured poly-Si thickness variation was then converted to an equivalent α-Si thickness change (Fig. 9). Although an oxide measurement is much simpler due to its simple optical model, poly-Si was selected at the cost of measurement speed because it has similar etch characteristics to α-Si. Our experimental results showed

that the long-term oxide to α-Si etch selectivity drift (3σ) was approximately 11 % of the average etch selectivity (6.5), whereas n-doped poly-Si to α-Si etch selectivity drift was only 2.5 % of the average etch selectivity (0.91). The initial α-Si thickness was measured by a SP (Spectra Photometer) before the etch.

The problems which emerged from the use of n-doped poly-Si for the estimation of α-Si thickness are slow measurement speed and a time delay coming from the film thickness extraction. The reliable measurement speed of n-doped poly-Si in real time, with the concurrent extraction of film thickness from the collected ellipsometrc data, was approximately 0.4 Hz. At the given 0.4 Hz measurement speed, we observed about a 10 nm change of n-doped poly-Si in every measurement under nominal etch conditions. This only provided approximately 9.1 nm of α-Si thickness estimation resolution, assuming constant etch selectivity. Accurate determination of film thickness is further complicated by the time delay inherent in obtaining data from two discrete sources: hardware and software. The RTSE system involves an approximate 0.18 sec time delay to acquire ellipsometric data. This hardware delay reflects the elapsed time in which the reflected light is acquired by the IPDA and transformed into the ellipsometric data format required for the optical model fitting. The software delay, on the other hand, originates from the process of matching the collected ellipsometric data to the optical model of the film layers. The amount of delay depends on the variation of film thickness between measurements and the complexity of the film's optical model. We solved these problems by implementing a Kalman-Bucy filter including a model-based algorithm which compensates for the time delay.

A. Kalman-Bucy Filter Development and Implementation

The Kalman-Bucy filter is a very efficient, easy to use, recursive least-squares filter. In order to determine the poly-Si thickness variation accurately under poor measurement resolution, we built a simple model based on the assumption that the etch rate of poly-Si is a constant, but unknown [20, 21]:

$$\dot{d} = \text{etch rate} = \text{constant}, \tag{3}$$

where d is the actual poly-Si thickness. Then, the model is:

$$\begin{aligned} \ddot{d} &= 0 + v \\ y &= d + w \end{aligned} \tag{4}$$

where v is white gaussian noise, w is measurement noise, and y is the measured poly-Si thickness. The

state equations are given in vector matrix form as:

$$\begin{aligned} \dot{x}_t &= Ax_t + Gv_t &= \begin{bmatrix} 0 & 1 \\ 0 & 0 \end{bmatrix} x_t + \begin{bmatrix} 0 \\ 1 \end{bmatrix} v_t \\ y_{t_k} &= Cx_{k_t} + w_{t_k} &= \begin{bmatrix} 1 & 0 \end{bmatrix} x_{t_k} + w_{t_k} \end{aligned} \tag{5}$$

where subscript t denotes continuous time and t_k denotes discrete time. The state vector x_t consists of two states, $x_t = [x_{1t} \;\; x_{2t}]$ =[film thickness etch rate]. State and measurement noise, v_t and w_{t_k}, are both modeled as independent, zero mean Gaussian with 0.154 variance for v_t and 150.7 variance for w_t. The state equation is a linear continuous-time system as opposed to the output (measurement) equation which is a discrete-time, linear observation taken at time instant t_k. Between measurements, the optimal (minimum variance) filter for the continuous-discrete system (5) satisfies the differential equations [22]:

$$\begin{aligned} \frac{d\hat{x}_t^t}{dt} &= A\hat{x}_t^t \\ \frac{dP_t^t}{dt} &= AP_t^t + P_t^t A' + GQG', \qquad t_k \le t < t_{k+1} \end{aligned} \tag{6}$$

where $'$ denotes matrix transpose. And at measurement t_k:

$$\begin{aligned} \hat{x}_{t_k}^{t_k^+} &= \hat{x}_{t_k}^{t_k^-} + K(t_k)(y_k - C\hat{x}_{t_k}^{t_k^-}) \\ P_{t_k}^{t_k^+} &= P_{t_k}^{t_k^-} - K(t_k)CP_{t_k}^{t_k^-} \end{aligned} \tag{7}$$

with a Kalman-Bucy gain:

$$K(t_k) \triangleq P_{t_k}^{t_k^-} C' [CP_{t_k}^{t_k^-} C' + R_{t_k}]^{-1} \tag{8}$$

where $\hat{x}_t^\tau$ is a conditional mean of the state x at time t given all measurements y on the interval $[0, \tau]$, P is the covariance matrix of states x, Q is the variance of state noise, and R is the variance of measurement noise, and $R > 0$. Equation (6) can be approximated by the discrete solution as follows. Between measurements:

$$\begin{aligned} \hat{x}_{k+1}^k &= \begin{bmatrix} 1 & T \\ 0 & 1 \end{bmatrix} \hat{x}_k^k \\ P_{k+1}^k &= \begin{bmatrix} 1 & T \\ 0 & 1 \end{bmatrix} P_k^k \begin{bmatrix} 1 & 0 \\ T & 1 \end{bmatrix} + GQG' \end{aligned} \tag{9}$$

and at measurement:

$$\begin{aligned} \hat{x}_k^k &= \hat{x}_k^{k-1} + K(k)(y_k - C\hat{x}_k^{k-1}) \\ P_k^k &= P_k^{k-1} - K(k)CP_k^{k-1} \end{aligned} \tag{10}$$

where x_k is the state at t_k, T is the time interval between two measurements which was set to 2.5 sec in this experiment, and:

$$K(k) = P_k^{k-1} C' [C P_k^{k-1} C' + R_k]^{-1}. \tag{11}$$

Figure 10 illustrates when the RTSE measurement occurs and new measured thickness information is available. If there were no time delay in the thickness extraction from the collected ellipsometric data, new thickness information would be available as soon as the measurement has occurred and could be used immediately to update the Kalman-Bucy gain (K) and covariance matrix (P). However, to compensate for the time delay, we needed to trace two time variables: t_s, the time when the most recent measurement occurred, and t_k, the time the most recent Kalman-Bucy gain was updated. As can be seen in Fig. 11, the Kalman-Bucy filter checks the time stamp and thickness information at an estimation interval of 0.1 sec. When new film thickness measurement (collecting only ellipsometric data) occurs, the time stamp generated at that same moment is stored in t_s. Due to the optical model fitting delay, however, new thickness information is updated with a delay of approximately 1.5-1.7 sec. When the new thickness information is updated, the Kalman-Bucy gain, covariance matrix (P) and current states are all updated. For instance, in Fig. 10, at time t_1, a new measurement has occurred, yet, the extracted thickness is only available at time t_2; the time interval, $t_2 - t_1$, is the elapsed time for the film thickness extraction. When new thickness information (d_2) is available at t_2, the new thickness d_2 is compared to the estimated thickness from the Kalman-Bucy filter, and then, the Kalman-Bucy gain and covariance matrix P are adjusted. After the update, the Kalman-Bucy filter continues to estimate the film thickness at a 0.1 sec time interval until subsequent thickness information becomes available. This iteration is continued until the endpoint is detected. The Kalman-Bucy filter was implemented as a MATLAB program and tested using actual n-doped poly-Si etch data. After verification of the filter performance, the code was converted into a LabVIEW program running on a PC and used for the endpoint detection of ME. The experimental results are presented in the following section. The MATLAB code is available in the APPENDIX.

B. Blank Wafer Endpoint Detection Experiment

B.1 Vacuum Grease Effect

Due to the difficulty of the mass production of a patterned sample by electron-beam lithography, a small piece of patterned sample was etched. A silicon-based vacuum grease was used to attach a 2×2 cm patterned sample on a six-inch silicon carrier wafer. The grease serves a dual purpose, providing

mechanical stability as well as good thermal conductivity between the sample and the silicon carrier wafer. It is important to note that the etch result for a vacuum grease applied small patterned sample, such as ours, may differ from the etch achieved on a patterned six-inch wafer. Therefore, it is necessary to verify that the experimental result obtained from a small sample with vacuum grease are valid for a six-inch production line wafer. We elected to focus on comparing etch rate since our etch profile control is based on film thickness estimation. Two α-Si samples, 2×2 cm in size, were pasted on a six-inch silicon carrier wafer and etched (Fig. 12). Then, the etch depth of each sample was measured. We assume that the plasma is uniformly distributed on both samples and that the etch rate difference is only affected by the vacuum grease. The average difference of etch depth between the two samples was 1.35 nm/min with a 1.05 nm standard deviation (σ). After that, a six-inch α-Si wafer was etched under the same etch condition. This wafer had the same film layers as the previously etched α-Si sample: 400 nm of α-Si on 5 nm of gate oxide. The same points were measured as in the previous experiment, and the result showed 1.05 nm/min etch difference between the two positions with 0.7 nm standard deviation. In terms of the etch non-uniformity, 0.3 nm/min etch rate variation resulting from the vacuum grease can be considered insignificant compared to the typical etch rate of 207 nm/min in the ME. Thus, we conclude that the result of our experiment conducted on a small patterned sample can be transferred to a patterned six-inch wafer.

B.2 Blank poly-Si and α-Si Endpoint Detection

To determine the performance of the endpoint detection system, two sets of experiments were conducted. In the first experiment, using the Kalman-Bucy filter, we set the endpoint detection system to stop the ME of a blank n-doped poly-Si sample etch when 200 nm of poly-Si was etched. Figure 13 illustrates the result of a blank n-doped poly-Si endpoint detection experiment. The square dots are the RTSE measurement of the poly-Si thickness and the dotted line is the estimated thickness at the 0.1 sec estimation intervals of the Kalman-Bucy filter. The estimated etch rate fluctuation, shown as a dashed line, is evidence of the well-known oscillations of etch thickness caused by the imperfect reflection index model of poly-Si. The gap between estimated and measured thickness represents a time delay of 1.4-1.7 sec, which corresponds to 6-7 nm difference in thickness. Over repeated tests, we were able to detect the endpoint of blank poly-Si in ME to within 1 nm accuracy.

The second set of experiments was conducted to determine the accuracy of α-Si endpoint detection by observing variation of n-doped poly-Si thickness and estimation of α-Si thickness based on the etch

selectivity. As shown in Fig. 14, a 2×2 cm blank α-Si sample was placed beside an n-doped poly-Si sample and then etched. The thickness of the α-Si sample, before and after etch, was measured by a SP. The etch results in closed-loop configuration employing an endpoint detection system and open-loop (timed) configuration are compared in Fig. 15. In the closed-loop configuration, the endpoint detection system was programmed to terminate the etch when 200 nm of α-Si was etched. On the other hand, in the open-loop configuration, the ME time was set to 58.2 sec which is the average etch time to etch 200 nm of α-Si under nominal etch conditions. The average etch depth of the closed-loop etch was 200.7 nm compared to 197.5 nm of the open-loop etch. Etch depth drift was significantly reduced with the use of endpoint detection system from 10.3 nm in open-loop etch to 3.9 nm in closed-loop etch.

C. Disturbance Rejection

Though a random disturbance can seriously compromise stability in the etching process and contribute to deterioration of device yield, an intentional disturbance is a useful tool in determining the robustness of a control system. To verify the robustness of our endpoint detection system, we intentionally introduced chemical and physical disturbances into a standard ME. The chemical disturbance consisted of changes in the chemical composition or the concentration of the plasma, whereas the physical disturbance consisted of changes in intensity of ion bombardment energy. In the first experiment employing a chemical disturbance, a chamber was vented and exposed to the atmosphere, and then cleaned with hydrogen peroxide (H_2O_2) and IPA. In the second experiment, a chemical disturbance was introduced by intentionally changing the Cl_2 flow rate by +5 sccm. And, in the last experiment, a physical disturbance was introduced by changing the bias power by -15 %, decreasing ion bombardment intensity, which in turn decreases the etch rate. In all cases, the endpoint detection system was set to stop the ME when 200 nm of α-Si was etched which takes 58.2 sec under nominal etch conditions.

The performance of the endpoint detection system in the presence of a chamber venting disturbance (the first experiment) is presented in Fig. 16. A significant decrease in the etch rate was observed for the first several etches. The absorbed water vapor in the chamber walls evaporates and oxidizes the silicon wafer surface. The extensive oxidation of the α-Si surface may retard the etch process resulting in a decreased etch rate. However, as the etch proceeds, the absorbed water vapor becomes exhausted, and therefore, the chamber condition returns to normal. To etch 200 nm of α-Si, the initial 68 sec of ME was reduced to about 59.5 sec after 7 repeated etches. The average closed-loop etch depth was maintained at 201.1 nm and a 3σ of 11.4 nm, as opposed to the open-loop etch depth with an average

of 186.7 nm and a 3σ of 30.3 nm. As demonstrated here, the etch process employing an endpoint detection system is obviously superior to the conventional timed etch in its ability to respond to and correct a venting disturbance.

In the second experiment, a chemical disturbance was introduced by increasing the chlorine flow rate by 5 sccm. The chamber pressure was kept fixed, forcing the chlorine concentration in the plasma to increase. The high reactivity of chlorine to silicon and the increased proportion of chlorine in the plasma serve to increase the vertical and lateral etch rates. An approximate increase of 6 % in the proportion of chlorine in the total gas flow rate increases the α-Si vertical etch rate by 5 %. To compensate for the increased etch rate, the endpoint detection system terminated the ME approximately 2.3 sec earlier than the average of 58.2 sec under standard ME conditions (Fig. 17). Although the closed-loop etch provides tighter control of etch depth, it has an etch depth bias of about 7 nm. The etch depth bias may come from the changed etch selectivity of poly-Si over α-Si under the chemical disturbance. As mentioned before, the estimation of α-Si etch depth is based on the poly-Si etch depth measurement and etch selectivity. The α-Si sample used in this experiment has a different crystal structure and phosphorus doping concentration from the n-doped poly-Si sample. Therefore, the etch rate change of n-doped poly-Si may be different from the etch rate of α-Si resulting in changed etch selectivity. Thus, the variation of the etch selectivity of n-doped poly-Si over α-Si under disturbance, which was assumed to be a fixed number, may cause the bias.

For the third and last experiment, a physical disturbance was created by decreasing the bias power by 15 % to simulate a power transmission mismatch in a matching network. Decreased bias power reduces the ion bombardment intensity, which reduces the etch rate of both poly-Si and α-Si. The effect of decreased bias power on the etch rate is illustrated in Fig. 18. The open-loop etch had an average etch depth of 192.8 nm for 58.2 sec of ME. However, the closed-loop endpoint detection scheme worked well under the severe bias power disturbance, achieving an average etch depth of 201.1 nm with a 3σ of 4.9 nm. To compensate for the decreased etch rate, the closed-loop endpoint detection system extended the ME time from the typical 58.2 sec to 60.7 sec.

V. Application of Endpoint Detection

In the previous section, we presented that a closed-loop etch employing an endpoint detection system with an RTSE and a Kalman-Bucy filter improves the control of etch depth and etch depth variation over the conventional open-loop (timed) etch system, with or without the presence of an intentional

disturbance. The previous experiments were performed on blank wafers, yet our goal was to improve the production reliability of an etch profile. We therefore moved on to the etch of patterned samples. First, we used a patterned sample with 100/400/5 nm of an oxide mask/α-Si/gate oxide structure. With this sample etch, we intentionally introduced the disturbances described in the previous section. The endpoint detection system was set to terminate the ME when 207 nm of α-Si was etched, then the timed OE continued to etch the rest of the α-Si. Next, we cut the α-Si thickness to 200 nm to simulate industry parameters and etch near to the gate oxide.

A. 0.1 μm, 400 nm thick n-doped α-Si Gate Etch

We first etched a 0.1 μm patterned sample under the standard etch conditions without disturbance: 10/60/100 sec of BT/ME/OE. A 60 sec of ME etches approximately 207 nm of α-Si under the standard etch conditions. This standard etch profile was used to measure the influence of the disturbance on the etch profile. Then, in the ME, we intentionally introduced a disturbance of a 50 % increase in Cl_2 flow rate. In the closed-loop etch, we aimed to stop the ME when the etched α-Si etch depth reached 207 nm, and then proceeded to the OE to etch the rest of the α-Si. On the other hand, in the open-loop etch, the patterned sample was etched for 10/60/100 sec of BT/ME/OE under the same disturbance as in the ME. Figure 19 illustrates the etch profile of standard, open-loop, and closed-loop etches. A 15 sec dip in BHF was employed to etch any residual oxide etch mask and re-deposited oxide-like materials on the wafer surface. The undercut at the gate bottom was produced during this BHF dip. Due to the increased chlorine flow rate, the lateral etch was enhanced resulting in worsened undercut under the oxide etch mask. In the closed-loop etch, the ME was terminated earlier than 60 sec to compensate for the increased etch rate, and thus it reduced the duration of the lateral etch. The CD at the gate top was 72 nm in the standard etch, 48 nm in the open-loop etch, and 67 nm in the closed-loop etch. The CD at the gate bottom was 113 nm in the standard etch, 76 nm in the open-loop etch, and 106 nm in the closed-loop etch. It is clearly shown in Fig. 19 that the closed-loop etch profile is more similar to the standard etch than the open-loop etch (see Table III).

B. 0.1 μm, 200 nm thick n-doped α-Si Gate Etch

In this experiment, we decreased the α-Si thickness to 200 nm, aiming to produce a 2:1 aspect ratio gate structure. By changing the gate thickness to 200 nm, we simulated a standard etch condition in the semiconductor manufacturing industry: etch near to a gate oxide in ME. At this juncture, we attempted to etch 190 nm of 200-nm thick α-Si during the ME, which takes approximately 55 sec. A

standard etch without any disturbance for 10/55 sec of BT/ME was conducted to check any etch profile drift and to provide a baseline. Then, an open-loop etch for 10/55 sec of BT/ME was performed with a disturbance in the ME, a 50 % increase in the bias power. And, finally, a closed-loop etch employing endpoint detection was conducted under the same bias power disturbance. With increased bias power, the α-Si etch rate was increased because of the intensified ion bombardment. As shown in Fig. 20, the 5 nm of a gate oxide was fully etched in the open-loop etch, and furthermore, the etch proceeded to the silicon substrate resulting in a 220 nm gate height. In contrast, the closed-loop etch terminated the ME to compensate for the increased etch rate, resulting in the gate oxide being intact. The closed-loop etch profile under the bias power disturbance was comparable to that of the standard etch without disturbance. It should be noted that the rather large bias power increase was employed as a disturbance to demonstrate the etch profile repeatability. That is, under a mild increase in the bias power, an open-loop etch profile would not be as dramatically poor as the one obtained with a 50 % increase. Nonetheless, any possible bias power disturbance in the open-loop etch would adversely affect the gate and silicon substrate by permitting ion penetration through a thinner α-Si layer than that of a standard or closed-loop etch. Because of unavailability of the equipment that permits us to evaluate the more subtle influence created by the moderately increased bias power, we were forced to resort to a drastic bias power increase that produced gate oxide loss evident even in visual inspection. The gate width at the top and bottom in the standard etch were 93 nm and 108 nm respectively, as opposed to 54 nm and 93 nm in the open-loop etch, and 77 nm and 93 nm in the closed-loop etch. The narrow gate width has mainly caused by the erosion of the oxide etch mask which was increased by the severe ion bombardment. This is due to the strong dependence of the oxide etch on ion bombardment energy.

To verify the robustness of the developed ME endpoint detection system, a validation experiment was conducted one year later. As a disturbance source, the same amount of Cl_2 or bias power disturbance was used to etch 4:1 and 2:1 aspect ratio gate structures, respectively. As shown in Table IV, the closed-loop etches under disturbance always achieved better etch results than the open-loop etches.

VI. Conclusion

In this paper, we investigated the etch profile control of a high-aspect ratio, 0.1 μm α-Si gate structure. Since the main etch time is critical to the final etch profile, we focused on the detection of the transition timing from ME to OE. For this, an endpoint detection of α-Si was developed with

the use of a Kalman-Bucy filter and a real-time spectroscopic ellipsometer to observe n-doped poly-Si thickness in real-time. We demonstrated the robustness of our endpoint detection technique under physical and chemical etching disturbance environments. Finally, our endpoint detection system was applied to 0.1 μm patterned α-Si gate etch. It was proven that the accurate transition timing control from ME to OE improves the etch profile reproducibility.

Appendix

I. M-file for Endpoint Detection

```
function [endtime,states,K]=
endpoint_delay(data,estimation_step,desired_depth);

% Kalman-Bucy filter MATLAB code for etch endpoint detection
% via film thickness estimation compensating time delay
% INPUTS:
% data =  [RTSE time stamp, film thickness]
% estimation_step - time interval to estimate the film thickness
% desired_depth - desired film thickness to stop etching
% OUTPUTS:
% endtime - the time when etch stopped
% states - estimated states when etch stopped
% K - Kalman-Bucy filter gain
% MODEL:
% X_dot=A*X+G*B
% y=C*X+w
% A=[1 0;0 0], X=[x_1;x_2], where x_1 is film thickness and x_2 is etch rate
% G=[0;1], B=[1 0] is 2 dimensional noise
% C=[1 0], y=x_1, film thickness
% w is measurement noise
% programmed by H.-M. Park and J. W. Grizzle
```

```
%%%%%%%% INITIALIZATION

B=[1 0]; G=[0;1];
% Variance of etch rate and measurement noise
Q=0.154; R=150.7;

% States of the system
x_hat_k=[data(1,2);-3.6];
x_hat_new=[data(1,2);-3.6];
d_hat=data(1,2);

% Initialize the current covariance matrix of x and Kalman-Bucy gain
P_cur=[140 0;0 0.22]; K_cur=[1.5;1.0];

% Initialize the time of the most recent data is taken
t_s=0.0;
% Initialize the time of the Kalman-Bucy filter gain was updated
t_k=0.0;
% Initialize the RTSE_time, the RTSE generating time stamp
RTSE_time_old=data(1,1);
% Initialize the RTSE_thickness, the RTSE measured thickness
RTSE_thickness_old=data(1,2);
% Initialize the counter
i=0;

%%%%%%%% ETCH DEPTH ESTIMATION

% Continue the estimation until the desired etch depth reaches
while (d_hat > desired_depth)
i=i+1;
```

```
t=estimation_step*i;

% Load next RTSE_time and RTSE_thickness from data file
RTSE_time_new=data(i,1); RTSE_thickness_new=data(i,2);

if (i==1)
RTSE_time_old=data(i,1); RTSE_thickness_old=data(i,2);
else
RTSE_time_old=data(i-1,1); RTSE_thickness_old=data(i-1,2);

% If RTSE_time (time stamp) is updated, then save it to t_s
if (RTSE_time_new ~= RTSE_time_old)
t_s=t;
x_hat_old=x_hat_new;
end

% If RTSE_thickness is updated, then update t_k
if (RTSE_thickness_new ~= RTSE_thickness_old)
t_k_old=t_k;
t_k=t_s;

% Update the Kalman-Bucy filter gain, covariance matrix
K_new=P_old*B'*inv(B*P_old*B'+R); K(:,i)=K_new;
P_cur=P_old-K_new*B*P_old;
% Update current state
x_hat_k=x_hat_old+K_new*(RTSE_thickness_new-B*x_hat_old);
end

P_new=[1 t-t_k;0 1]*P_cur*[1 t-t_k;0 1]'+G*Q*G';
P_old=P_new;
x_hat_new=[1 t-t_k;0 1]*x_hat_k;
```

```
% Calculate estimated film thickness
d_hat=B*x_hat_new; state(:,i)=x_hat_new;
end

endtime=i;
return;
```

II. Acknowledgments

The authors sincerely thank T. Brock (University of Michigan) for help with the e-beam lithography. This work was supported in part by the Semiconductor Research Corporation under contract No. 97-FC-085, DARPA/AFOSR MURI Center under contract No. F49620-95-1-0524, and NIST Advanced Technology Program (ATP) under contract No. 70NANB8H4067.

References

[1] T. D. Bestwick and G. S. Oehrlein, "Reactive ion etching of silicon using bromine containing plasmas," *J. Vac. Sci. Technol.*, vol. A 8, no. 3, pp. 1696–1701, May/June 1990.

[2] L. Y. Tsou, "Highly selective reactive ion etching of polysilicon with hydrogen bromide," *J. Electrochem. Soc.*, vol. 136, no. 10, pp. 3003–3006, Oct. 1989.

[3] R. J. Hoekstra, M. J. Grapperhaus, and M. J. Kushner, "Integrated plasma equipment model for polysilicon etch profiles in an inductively coupled plasma reator with subwafer and superwafer topography," *J. Vac. Sci. Technol.*, vol. A 15, no. 4, pp. 1913–1921, July/Aug. 1997.

[4] P. D. Hanish, *Phenmenological Modeling of Reactive Ion Etching for Real-Time Feedback Control*, Ph.D. thesis, Univ. of Michigan, 1996.

[5] M. J. Kushner, "Advances in plasma equipment modeling," *Solid State Tech.*, vol. 39, no. 6, pp. 135–144, June 1996.

[6] C. Spanos, "Statistical process control in semiconductor manufacturing," *Microelectronic Eng.*, vol. 10, no. 3-4, pp. 271–276, Feb. 1991.

[7] B. A. Rashap, M. E. Elta, H. Etemad, J. P. Fournier, J. S. Freudenberg, M. D. Giles, J. W. Grizzle, P. T. Kabamba, P. P. Khargonekar, S. Lafortune, J. R. Moyne, D. Teneketzis, and Jr. F. L. Terry, "Contol of semiconductor manufacturing equipment: Real-time feedback control of a reactive ion etcher," *IEEE Trans. Semicond. Manufact.*, vol. 8, no. 3, pp. 286–297, Aug. 1995.

[8] T. H. Smith, S. Boning, J. Stefani, and S. W. Butler, "Run to run advanced process control of metal sputter deposition," *IEEE Trans. Semiconduct. Manufact.*, vol. 11, no. 2, pp. 276–284, May 1998.

[9] R. N. Castellano, "Profile control in plasma etching sio_2," *Solid State Tech.*, pp. 203–206, May 1984.

[10] R. H. Bruce, "Anisotropy control in dry etching," *Solid State Tech.*, pp. 64–68, Oct. 1981.

[11] P. Klimechy, D. Schweiger, and J. W. Grizzle, "Real-time data acquisition & feedback control solution for industrial plasma reactors," *Proc. Electrochem. Soc. Spring Meeting*, Seattle, WA, 1999.

[12] J. N. Hilfiker and R. A. Synowicki, "Spectroscopic ellipsometry for process applications," *Solid State Tech.*, vol. 39, no. 10, pp. 157–167, Oct. 1996.

[13] S. W. Butler and J. A. Stefani, "Supervisory run-to-run control of polysilicon gate etch using in situ ellipsometry," *IEEE Trans. Semiconduct. Manufact.*, vol. 7, no. 2, pp. 193–201, May 1994.

[14] S. Maung, S. Bannerjee, D. Draheim, S. Henck, and S. W. Butler, "Integration of in situ spectral ellipsometry with mmst machine control," *IEEE Tran. Semicond. Manufact.*, vol. 7, no. 2, pp. 184–192, May 1994.

[15] R. A. Synowicki, "Spectroscopic ellipsometry characterization of indium tin oxide film microstructure and optical constants," *Thin Solid Films*, vol. 313-314, no. 1-2, pp. 394–397, Feb. 1997.

[16] H. Arimoto, S. Nakamura, S. Miyata, and K. Nakagawa, "Monitoring of sram gate patterns in krf lithography by ellipsometry," *IEEE Trans. Semiconduct. Manufact.*, vol. 12, no. 2, pp. 166–169, May 1999.

[17] R. N. M. Azzam and N. M. Bashara, *Ellipsometry and Polarized Light*, Elsevier Science Publishing Co., North-Holland, Amsterdam, 1987.

[18] C. J. Mogab and T. A. Shankoff, "Plasma etching of titanium for application to the patterning of ti-pd-au metallization," *J. Electrochem. Soc.*, vol. 124, no. 11, pp. 1766–1771, Nov. 1977.

[19] D. Tennant, F. Klemens, T. Sorsch, F. Baumann, G. Timp, N. Layadi, A. Kornblit, B. J. Sapjeta, J. Rosamilia, T. Boone, B. Weir, and P. Silverman, "Gate technology for 70 nm metal-oxide-semiconductor field-effect transistor with ultrathin ($<$ 2 nm) oxide," *J. Vac. Sci. Technol.*, vol. B 15, no. 6, pp. 2799–2805, Nov./Dec. 1997.

[20] T. L. Vincent, P. P. Khargonekar, and Jr. F. L. Terry, "Extended kalman filtering-based method of processing reflectometry data for fast in-situ etch rate measurements," *IEEE Trans Semicond. Manufact.*, vol. 10, no. 1, pp. 42–51, Feb. 1997.

[21] C. G. Galarza, P. P. Khargonekar, N. Layadi, T. L. Vincent, E. A. Rietman, and J. T. C. Lee, "New algorithm for real-time

thin film thickness estimation given in situ multiwavelength ellipsometry using an extended kalman filter," *Thin Solid Films*, vol. 313-314, no. 1-2, pp. 156–160, Feb. 1997.

[22] A. H. Jazwinski, *Stochastic Processes and Filtering Theory*, vol. 64 of *Mathematics in Science and Engineering*, Academic press, New York, NY, 1970.

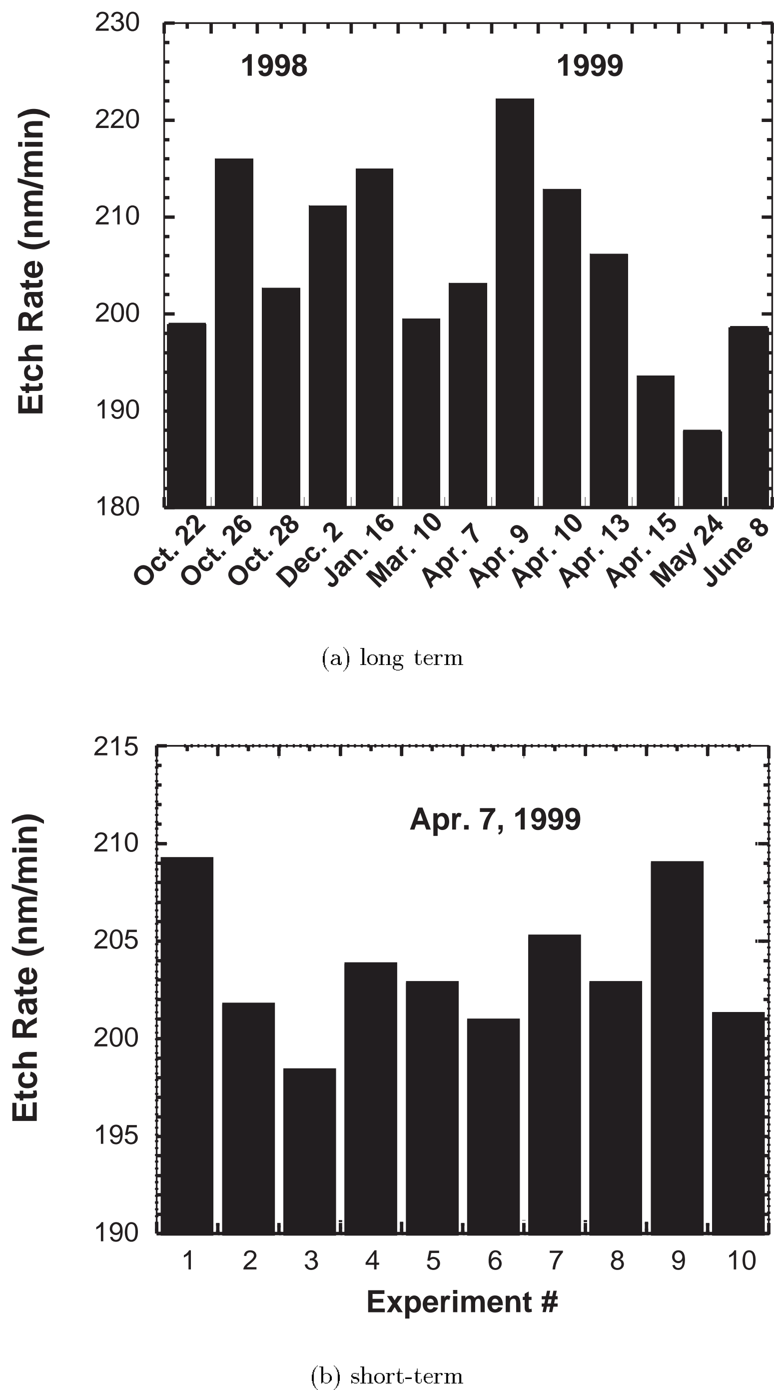

(a) long term

(b) short-term

Fig. 1. Long-term (over eight months) and short-term (within one hour) α-Si etch rate drift with the use of a Lam TCP 9400SE plasma etching system.

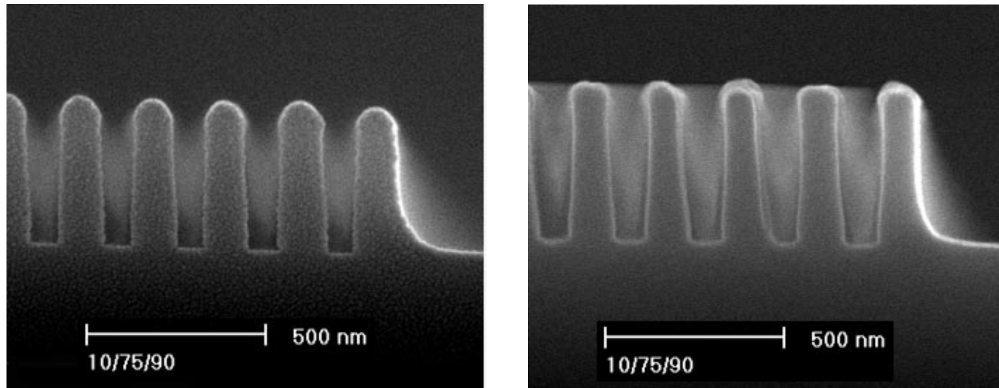

(a) July 18, 1998

(b) July 27, 1998

Fig. 2. Cross-sectional etch profile of 0.1 μm α-Si gate under 10/75/90 sec of BT/ME/OE in a Lam TCP 9400SE plasma etching system.

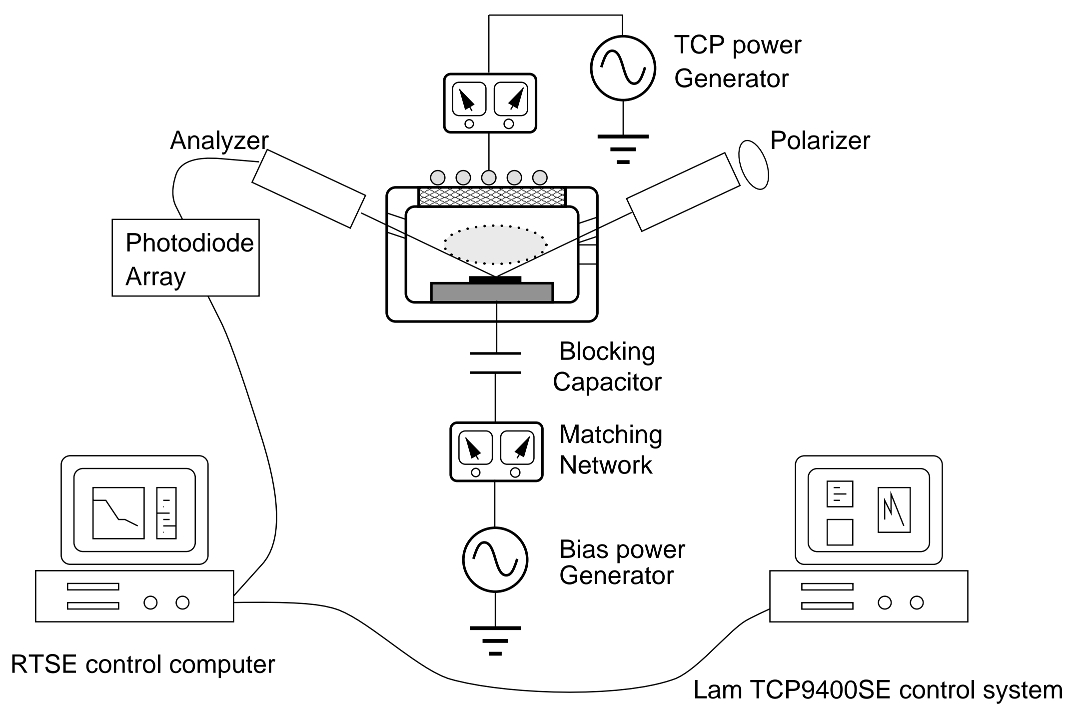

Fig. 3. Schematic of an experimental apparatus.

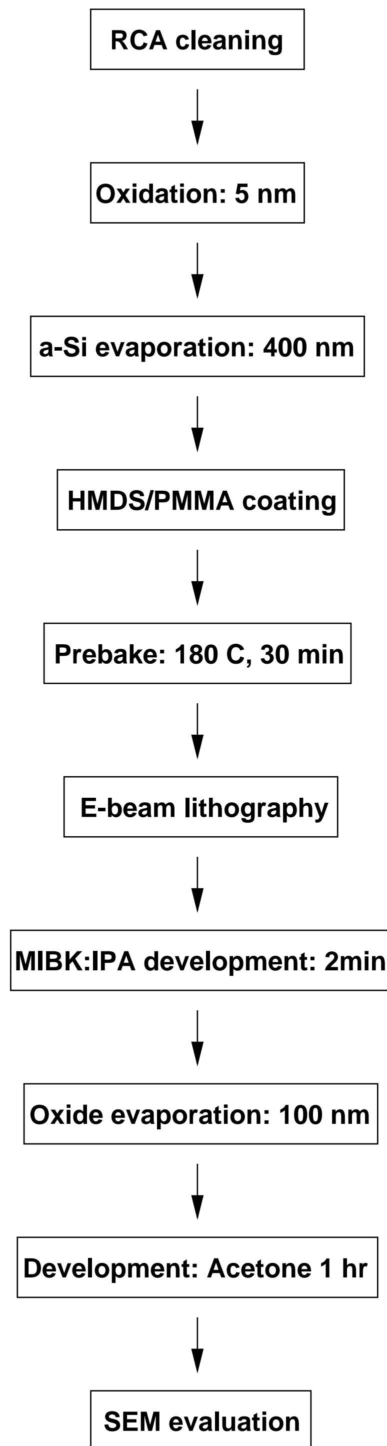

Fig. 4. 100-nm oxide etch mask patterning step employed in this study.

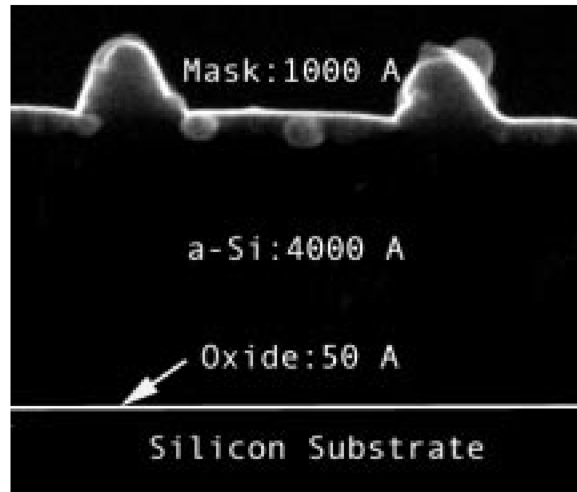

Fig. 5. SEM micrograph of 100-nm wide and 100-nm thick oxide etch mask.

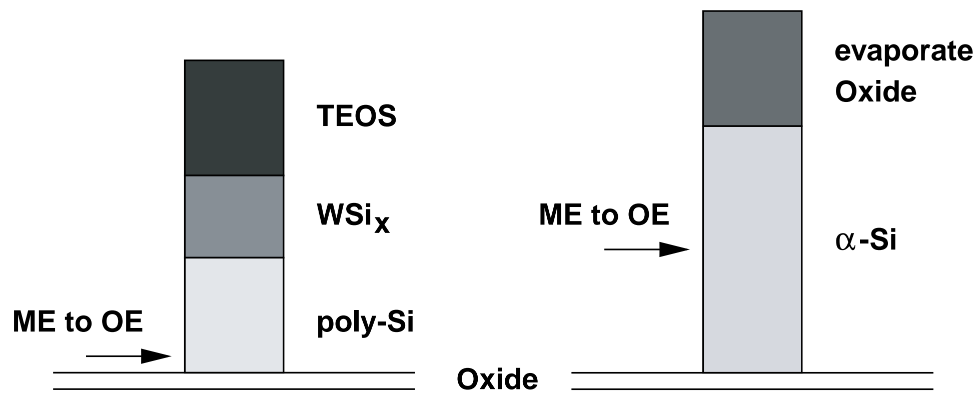

Fig. 6. Gate structures developed in the Bell Labs (left) [19] and the one used in this work (right). They are not drawn in scale.

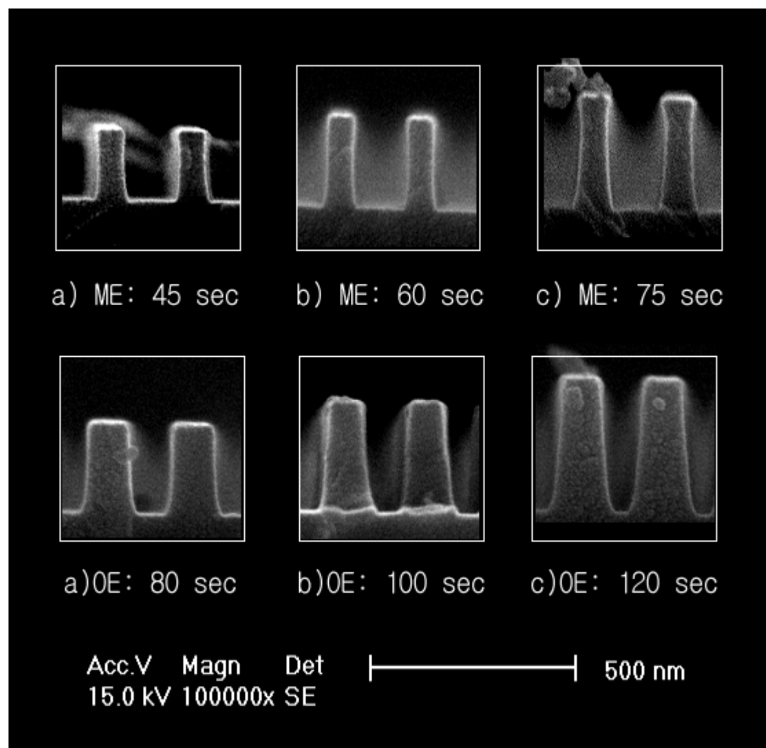

Fig. 7. Cross-sectional etch profile of various ME and OE etch times.

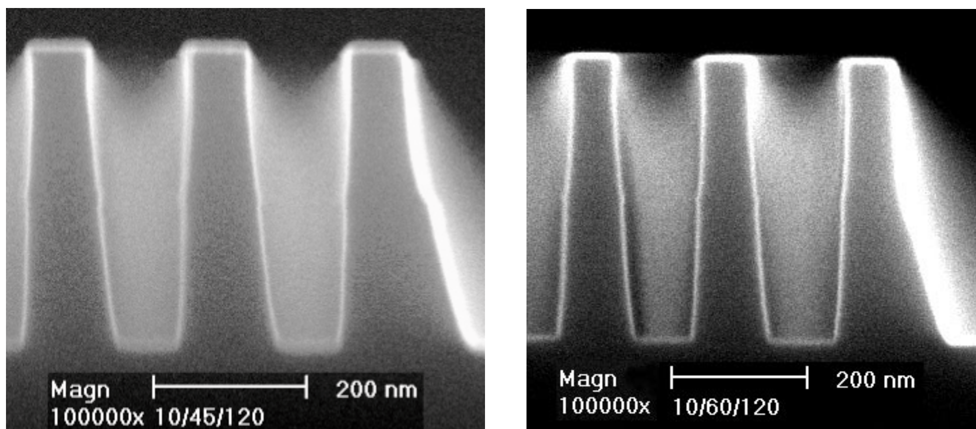

(a) 10/45/120 sec BT/ME/OE

(b) 10/60/120 sec BT/ME/OE

Fig. 8. Etch profile variation with different ME etch times: 45 sec vs. 60 sec.

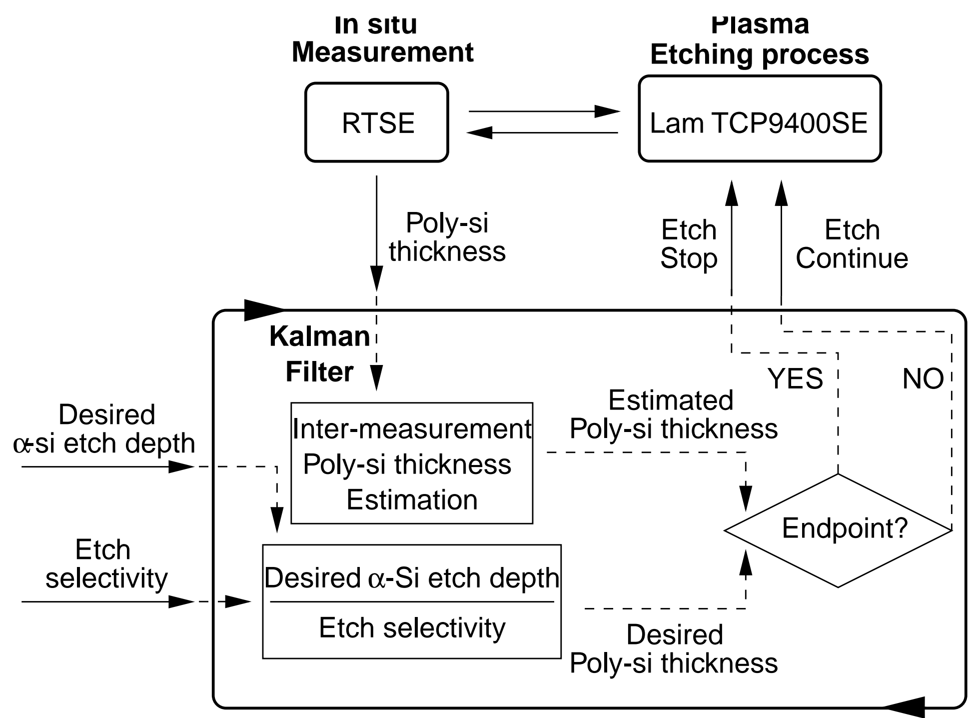

Fig. 9. Diagram of endpoint detection algorithm.

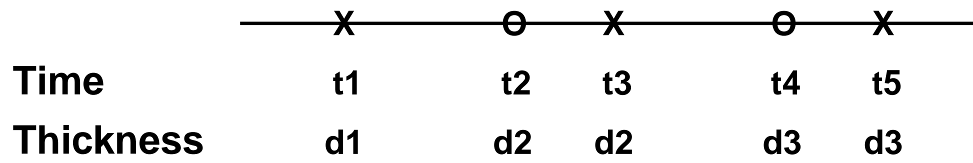

Fig. 10. Illustration of measurement time stamp and thickness information update via RTSE system. X represents measurement occurrence and **O** is when the new measured thickness information is available.

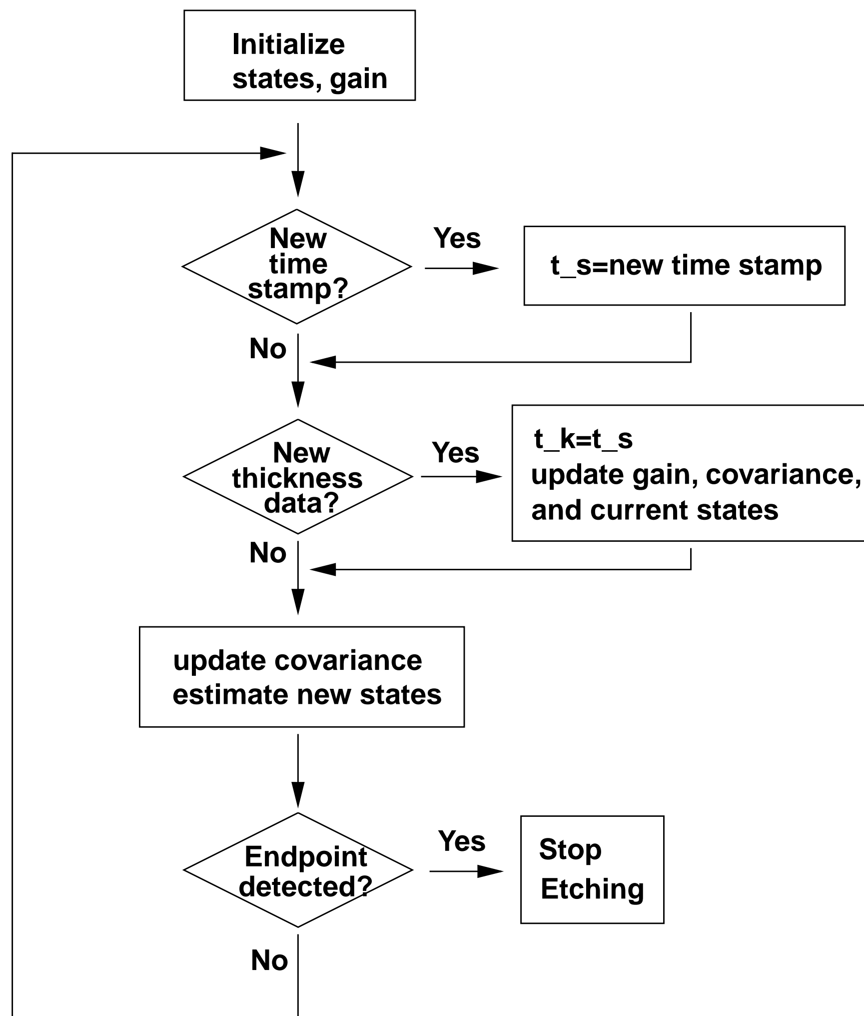

Fig. 11. Flow chart of film thickness estimation based on a Kalman-Bucy filter.

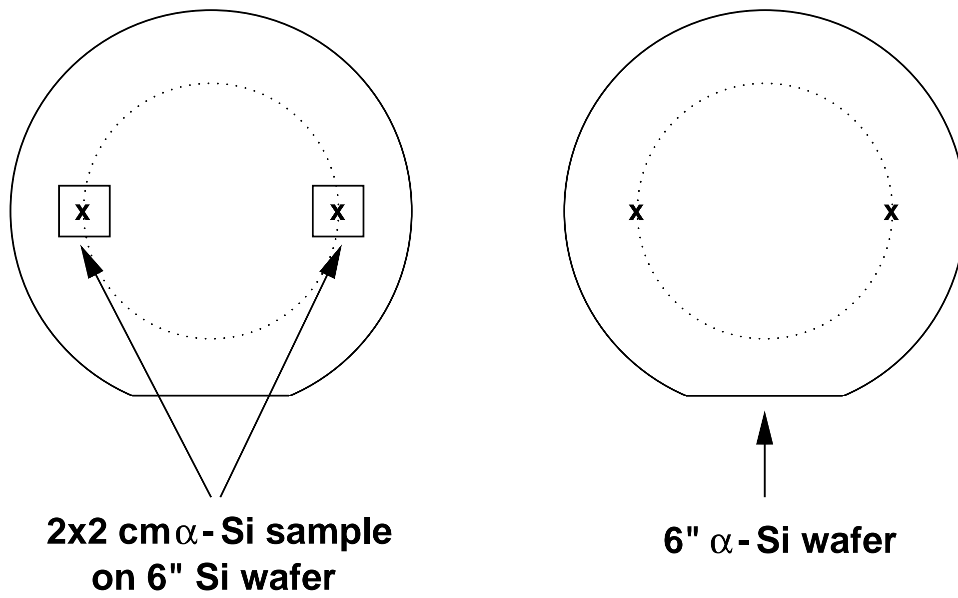

Fig. 12. Schematic of the wafers used in the vacuum grease disturbance experiments.

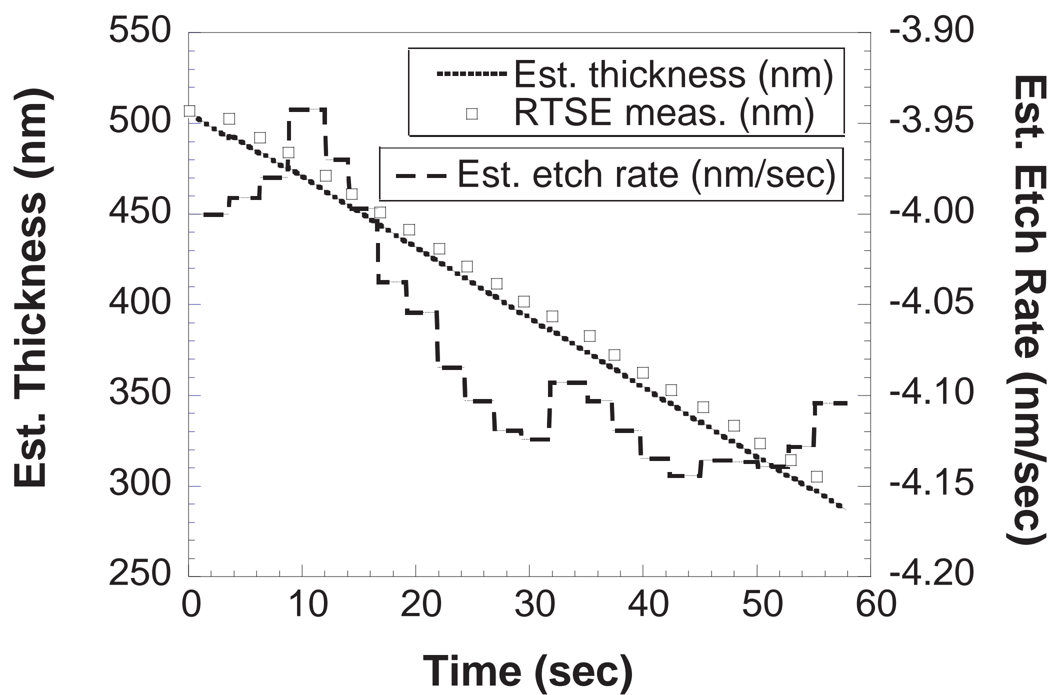

Fig. 13. Experimental result of the poly-Si endpoint detection with the use of a Kalman-Bucy filter.

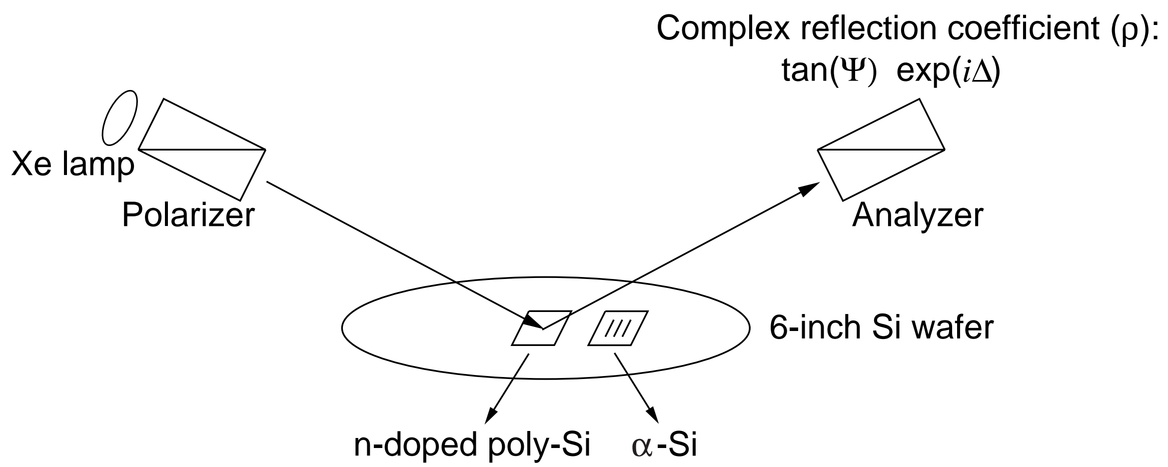

Fig. 14. Schematic of a blank n-doped poly-Si sample etch depth measurement to estimate the α-Si etch depth with the use of an RTSE system.

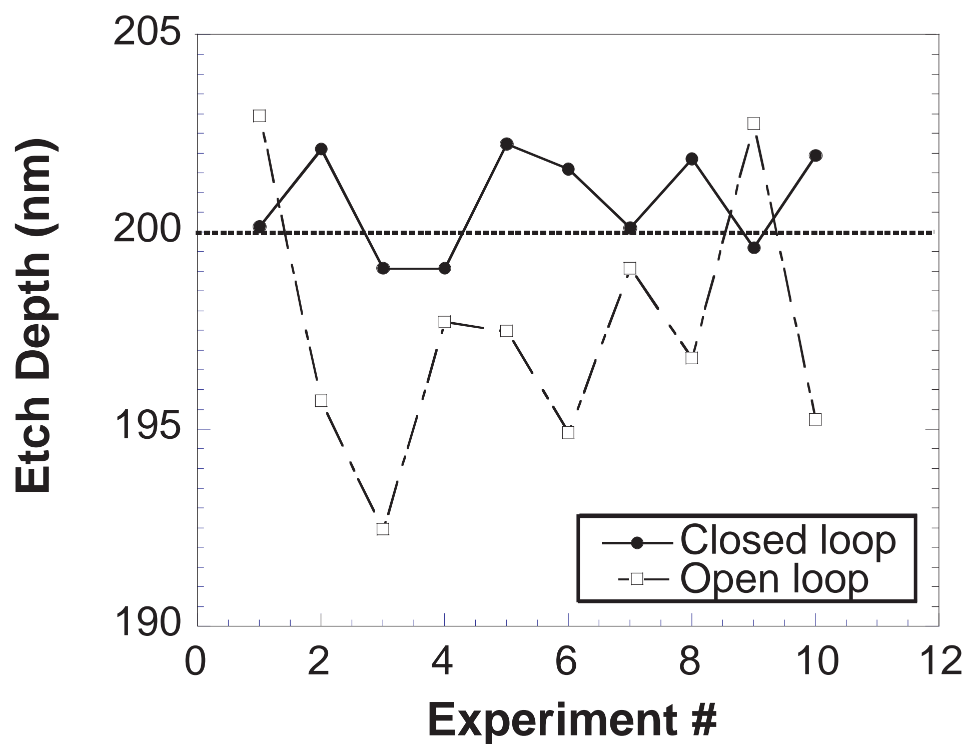

Fig. 15. Comparison of the closed-loop etch and open-loop (timed) etch of α-Si.

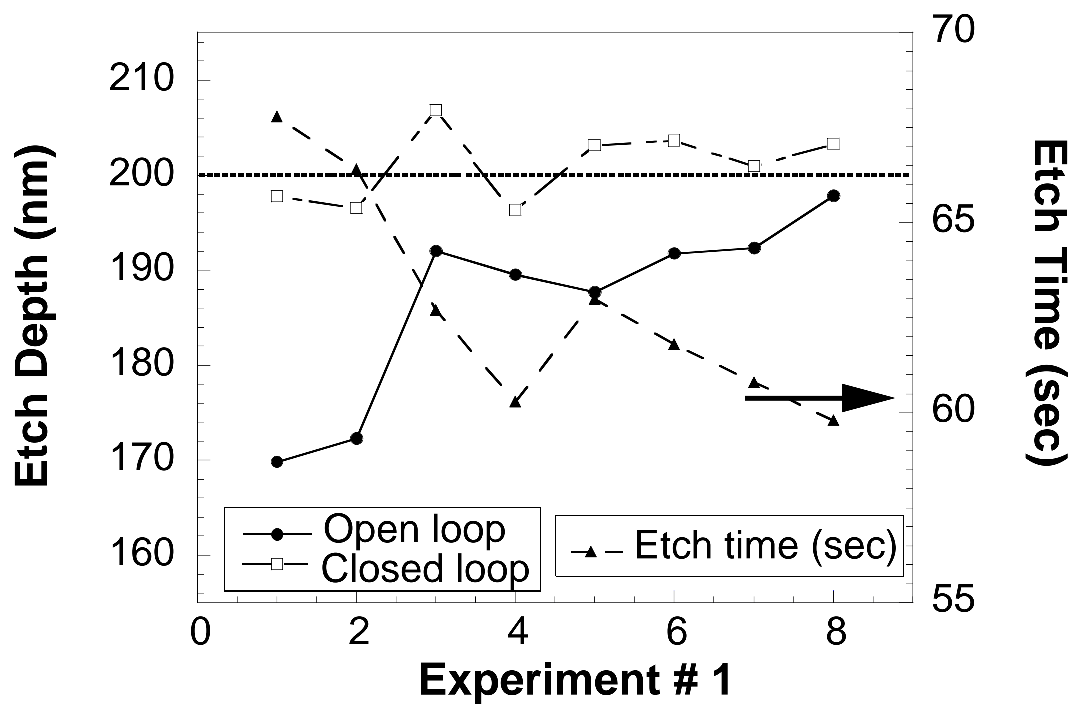

Fig. 16. Comparison of the closed-loop and open-loop (timed) etch under chamber venting disturbance.

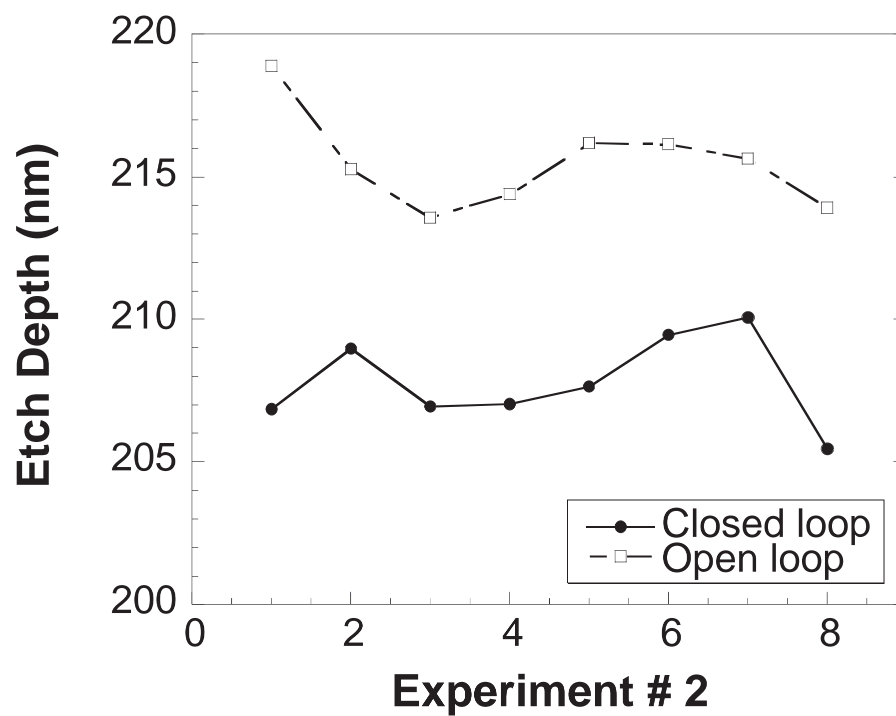

Fig. 17. Comparison of the closed-loop and open-loop (timed) etch under chlorine flow rate disturbance, +5 sccm.

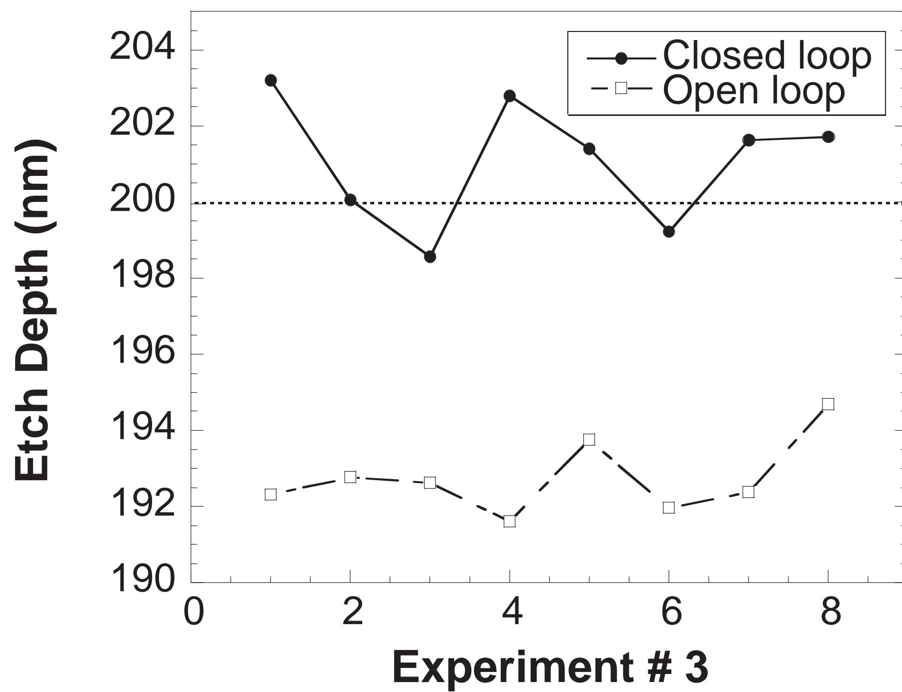

Fig. 18. Comparison of the closed-loop etch and open-loop (timed) etch under bias power disturbance, -15 %.

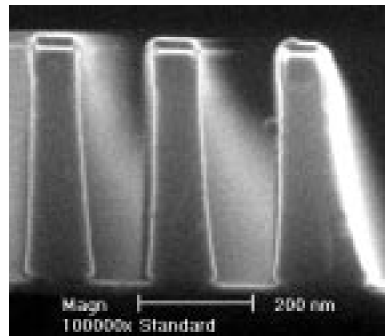

(a) Standard etch

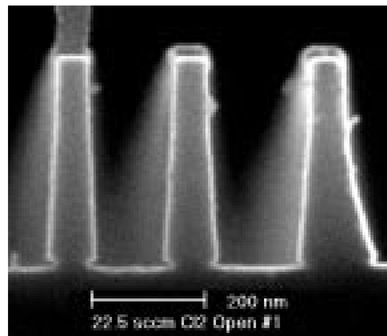

(b) Open-loop (timed) etch

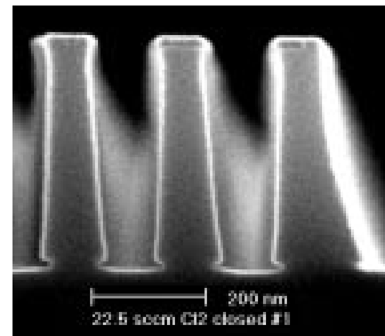

(c) Closed-loop etch

Fig. 19. Comparison of the open-loop and closed-loop etch profile under a 50 % increase of Cl_2 flow rate disturbance in ME.

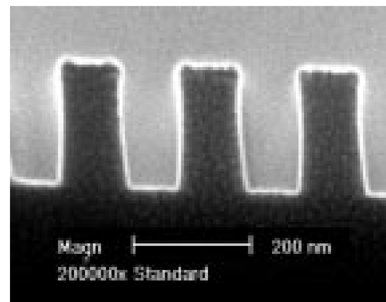

(a) Standard etch

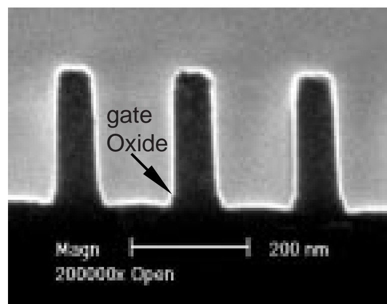

(b) Open-loop (timed) etch

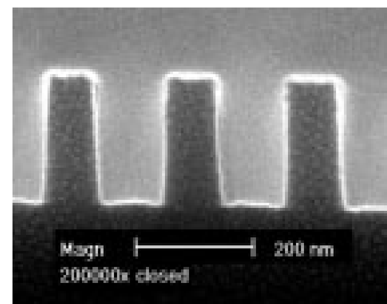

(c) Closed-loop etch

Fig. 20. Comparison of the open-loop and closed-loop etch profile under a 50 % increase of bias power disturbance in ME.

Etch step	BT	ME	OE
TCP power (W)	200	250	300
bias power (W)	40	180	200
Pressure (mTorr)	13	10	60
C_2F_6 (sccm)	100	0	0
Cl_2 (sccm)	0	15	0
HBr (sccm)	0	75	100
He (sccm)	0	0	200
O_2(20 %)+He(80 %) (sccm)	0	0	10

TABLE I

Etch recipe used for an n-doped α-Si gate-line etch in a Lam TCP 9400SE plasma etcher.

	Top	Bottom	Space
10/45/120 sec	67 nm	125 nm	75 nm
10/60/120 sec	55 nm	110 nm	90 nm

TABLE II

CD measurement of the two etch profiles with different ME time, 45 and 60 sec.

4:1 aspect ratio	Standard	Open-loop	Closed-loop
Top CD (nm)	72 nm	48 nm	67 nm
Bottom CD (nm)	113 nm	76 nm	106 nm
2:1 aspect ratio	Standard	Open-loop	Closed-loop
Top CD (nm)	93 nm	54 nm	77 nm
Bottom CD (nm)	108 nm	93 nm	93 nm

TABLE III

Measured CD of standard, open-loop, and closed-loop etch profile of 4:1 and 2:1 aspect ratio gate etch.

4:1 aspect ratio	Standard	Open-loop	Closed-loop
Top CD (nm)	84 nm	55 nm	77 nm
Bottom CD (nm)	135 nm	105 nm	124 nm
2:1 aspect ratio	Standard	Open-loop	Closed-loop
Top CD (nm)	113 nm	50 nm	90 nm
Bottom CD (nm)	128 nm	108 nm	119 nm

TABLE IV

Validation experimental result of the ME endpoint detection of 4:1 and 2:1 aspect ratio gate etch under disturbance.